

**Design and Characterization of a Low Cost Dual Differential Proving  
Ring Force Sensor Utilizing Hall-Effect Sensors**

by

Christopher W. Rivest

SUBMITTED TO THE DEPARTMENT OF MECHANICAL ENGINEERING IN  
PARTIAL FULFILLMENT OF THE REQUIREMENTS FOR THE DEGREE OF

BACHELOR OF SCIENCE IN MECHANICAL ENGINEERING  
AT THE  
MASSACHUSETTS INSTITUTE OF TECHNOLOGY

JUNE 2006

© 2006 Massachusetts Institute of Technology  
All rights reserved

Signature of Author \_\_\_\_\_

Department of Mechanical Engineering

May 12, 2006

Certified by \_\_\_\_\_

Ian W. Hunter

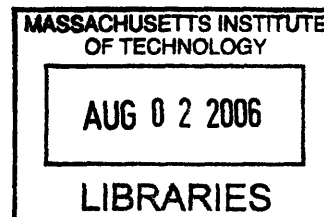
Hatsopoulos Professor of Mechanical Engineering

Thesis Supervisor

Accepted by \_\_\_\_\_

John H. Lienhard V

Chairman of the Undergraduate Thesis Committee, Mechanical Engineering



ARCHIVES

# **Design and Characterization of a Low Cost Dual Differential Proving Ring Force Sensor Utilizing Hall-Effect Sensors**

by

Christopher W. Rivest

Submitted to the Department of Mechanical Engineering  
on May 12, 2006 in partial fulfillment of the requirements  
for the Degree of Bachelor of Science in Mechanical Engineering

## **ABSTRACT**

A novel dual differential hall-effect based proving ring force sensor has been designed, manufactured, and tested. Strain gauge based force sensors are among the most common methods of measuring static and dynamic forces, yet they suffer from a wide array of negative attributes including: high cost due to signal amplification instrumentation, high temperature sensitivity, and only moderate dynamic range. The goal of the research herein described was to design and test a low cost, high dynamic range force sensor. Hall-Effect sensors have high bandwidth ( $>100$  kHz), a wide dynamic range, are low in cost ( $<0.5$  \$), and are ideally suited to dynamic and static force measurements. Proving rings - diametrically loaded hoops of metal, have long been used to measure force yet suffer many setbacks due to their historical designs utilizing mechanical and strain gauge methods of strain detection. A novel nested proving ring flexure has been combined with hall-effect sensors to fulfill the design requirements of a low cost and robust force sensor. Initial data demonstrates that the nested proving ring force sensor herein described is capable of resolving forces of in the range of 0 to 30 Newtons with an accuracy of 0.235 Newtons, all at a potential mass-manufactured cost of U.S. \$10.00 per unit.

Thesis Supervisor: Ian W. Hunter

Title: Hatsopoulos Professor of Mechanical Engineering

**Table of Contents:**

<b>1.0 INTRODUCTION.....</b>	<b>5</b>
<b>2.0 MOTIVATION AND BACKGROUND .....</b>	<b>5</b>
<b>2.1 IDAT .....</b>	<b>5</b>
<b>3.0 INSTRUMENT CONCEPT .....</b>	<b>6</b>
<b>3.1 Proving Ring Background .....</b>	<b>7</b>
<b>3.2 Prior Art in Proving Ring Force Sensors.....</b>	<b>8</b>
<b>3.3 Proving Ring Theory .....</b>	<b>9</b>
<b>3.4 Hall Effect Sensors and Theory.....</b>	<b>10</b>
<b>4.0 MECHANICAL DESIGN AND FEA ANALYSIS .....</b>	<b>12</b>
<b>4.1 Dual Differential Design.....</b>	<b>12</b>
<b>4.2 Novel Nested Proving Ring Design.....</b>	<b>13</b>
<b>5.0 DEVICE MANUFACTURE, TESTING, AND DATA .....</b>	<b>14</b>
<b>5.1 Hall-Effect Sensor Characterization.....</b>	<b>14</b>
<b>5.2 Circuit Board Design .....</b>	<b>17</b>
<b>5.3 Generation 1: Laser Cut 10mm Acrylic.....</b>	<b>18</b>
<b>5.4 Generation 2: 3D Printed Viper Resin .....</b>	<b>19</b>
<b>5.5 Generation 3: Wire EDM, Low Force Aluminum Proving Ring .....</b>	<b>20</b>
<b>5.6 Generation 4: Wire EDM, High Force Aluminum Proving Ring .....</b>	<b>20</b>
<b>6.0 EXPERIMENTAL SETUP .....</b>	<b>21</b>
<b>7.0 TESTING, DATA, AND ANALYSIS .....</b>	<b>22</b>
<b>7.1 Generation 2 Testing (3D Printed Sensor).....</b>	<b>24</b>
<b>7.2 Generation 3 Testing (Low Force Aluminum Sensor).....</b>	<b>25</b>
<b>6.4 Generation 4 Testing (High Force Aluminum Sensor).....</b>	<b>26</b>
<b>8.0 CONCLUSIONS AND FURTHER WORK.....</b>	<b>29</b>

**Table of Figures:**

Figure 1: Picture of a classic proving ring force sensor design [1] ..... 7

Figure 2: Diagram of the deformation of a diametrally loaded proving ring [1]..... 7

Figure 3: Proving Rings: Reed [1], Micrometer [2], and Strain Gauge [3]...... 9

Figure 4: A diagram of forces experienced by a diametrally loaded proving ring [4]. ..... 9

Figure 5: A diagram of the Hall-Effect [6]. ..... 11

Figure 6: Hall Effect Sensors [7]. ..... 12

Figure 7: Graphs of SS495A Hall Effect Sensor Characteristics [7]..... 12

Figure 8: Tabe of SS495A Hall Effect Sensor Characteristics [7]. ..... 13

Figure 9: Dual Differential Hall-Effect Proving Ring. .... 14

Figure 10: Novel Nested Proving Ring Design Solid Model ..... 14

Figure 11: FEA Analysis of Nested Proving Ring Design. .... 15

Figure 12: The D22 1/8<sup>th</sup> inch Rare Earth (NdFeB) Magnet [8]. ..... 15

Figure 13: Hall-Effect Sensor Characterization Setup..... 16

Figure 14: Characterization of the SS495A Hall-Effect Sensor. .... 17

Figure 15: SS495A Hall-Effect Sensor's Response to North and South Poles. .... 17

Figure 16: Circuit Board Design and Implementation..... 18

Figure 17: 1<sup>st</sup> Generation: Laser Cut Acrylic Nested Proving Ring. .... 19

Figure 18: 2<sup>nd</sup> Generation: 3D Printed Nested Proving Ring. .... 20

Figure 19: 3<sup>rd</sup> Generation: Wire EDM Manufactured Proving Ring. .... 20

Figure 20: 4<sup>th</sup> Generation: Wire EDM Manufactured Proving Ring. .... 21

Figure 21: Experimental Setup. .... 22

Figure 22: Close Up of Experimenal Setup ..... 22

Figure 23: Spring Model of Nested Proving Ring Design..... 23

Figure 24: Inverse Spring Constants for Outer and Inner Rings. .... 24

Figure 25: Displacement Vs. Load for 3D Printed Sensor . .... 25

Figure 26: Loaded Axis Displacement Vs. Load, 3D Printed Sensor. .... 25

Figure 27: Loaded Axis Displacement Vs. Load, Low Force Aluminum Sensor. .... 26

Figure 28: Plastically Deformed Low Force Proving Ring. .... 26

Figure 29: High Force Hall-Sensor Readings..... 27

Figure 30: Bi-Axial Deflection Vs. Load, High Force Sensor. .... 27

Figure 31: Non-Loaded Axis, Theoretical Vs. Actual Deflection. .... 28

Figure 32: Loaded Axis, Theoretical Vs. Actual Deflection. .... 28

## 1.0 Introduction

The ability to measure the world around us is fundamental to the advancement of science. Without the proper tools to measure and analyze the world, we would not have the immense capability that we do as a society to create change and advance the society as we know it. The ability to measure force in particular has been crucial to our understanding of physics and engineering. Furthermore by measuring forces we can gain a deeper understanding of the actions and reactions that occur in our daily lives, whether playing soccer, driving a car, or flying in an airplane.

The ability to measure force in an easy and intuitive manner is fundamental to any student's understanding of the world around them. Conventional strain and quartz based force sensors suffer from a variety of problems that make them poorly suited for use as an educational tool. Quartz based force sensors are unable to measure static forces while strain gauge based force sensors suffer from high cost, low bandwidth, and high temperature sensitivity.

The goal of this project was to develop a low cost, wireless force sensor that would be ideally suited to use in educational environments. To accomplish this goal, two previously uncombined technologies were combined in a fashion that suited the stated design requirements. Specifically, the unique combination of high bandwidth, low cost hall-effect sensors, mounted onto a nested proving-ring aluminum base, enabled the fulfillment of the design objectives.

## 2.0 Motivation and Background

The project described in this thesis was part of a suite of sensors being developed for educational and commercial use as part of the IDAT initiative. The IDAT initiative, in turn, is part of a much larger MIT initiative called the iCampus initiative. A brief description of the iCampus initiative is given below. [9]

The iCampus Outreach Initiative seeks to disseminate innovative educational technology tools that can make a significant, sustainable difference in how well and quickly students learn, how much they remember, and how fast they can shift from absorbing facts and concepts to creating new ideas and solutions themselves. With generous support from Microsoft Research, iCampus Outreach seeks faculty and institutions looking to adopt new educational tools. The Outreach project will provide the software tools, supporting documentation, and guidance to assist higher education institutions to successfully implement these tools.

### 2.1 IDAT

A brief summary of the IDAT project, taken from the IDAT website (<http://idat.mit.edu/>), is given below [10].

#### **Project Overview:**

The main goal of the IDAT project is to develop a suite of wireless sensors as educational tools to teach instrumentation and measurement but designed also to meet the precision and quality that is required in science and engineering

applications. Over 60 wireless sensors are being developed to cover all of the major areas of physical sciences, engineering, biology and medicine.

**Objectives:**

To develop a large set of high quality, yet low cost, sensors and actuators that are wireless and contain their own rechargeable energy source (battery/super capacitor) for use in a wide range of educational settings including universities, high schools, science museums as well as for personal (“home education”) use. The main purpose of the wireless sensors is to make it very simple for students to measure and then possibly control things of interest. Wireless sensor application examples include:

- measuring the 3D accelerations during ski jumping or acrobatics;
- recording the forces and 3D accelerations involved when tennis balls or baseballs are hit;
- monitoring heart rate, blood pressure and respiration rate during exercise;
- mapping the 3D magnetic field around a magnet;
- determining the heat capacity and thermal conductivity of a liquid;
- measuring the velocity of sound in air and other gases;
- evaluating the stiffness of various materials (including skin);
- analyzing the acoustic frequency spectrum of musical instruments;
- measuring the optical power density of light sources (including the sun);
- mapping the 3D electrical charge about objects;
- determining the force generating capability, speed and efficiency of motors and actuators;
- servo controlling linear Lorentz force actuators using wireless force and displacement sensors;
- guiding blindfolded students using wireless tactile skin actuators;
- determining the impact forces and 3D acceleration during interceptions in football;

### **3.0 Instrument Concept**

Although the IDAT initiative encompasses a wide array of sensors, the goal of this particular project was to design, manufacture, and analyze a force sensor. The stated requirements for the force sensor were that it should:

- a) be low cost (<\$10.00 per sensor)
- b) have a true, high voltage (1 V to 5 V), DC response, eliminating the need for costly amplification electronics
- c) be robust in design and withstand use in educational settings (high cyclical loading, misuse etc.)
- d) have a low noise output signal that is compensated to be temperature independent
- e) have a high bandwidth (>100 kHz)
- f) have a wide dynamic range (>100,000)

In the initial analysis of what type of design might fulfill these requirements, it was realized that a simple yet robust proving ring could be combined with low cost hall-effect sensors to satisfy all of the stated design requirements.

### 3.1 Proving Ring Background

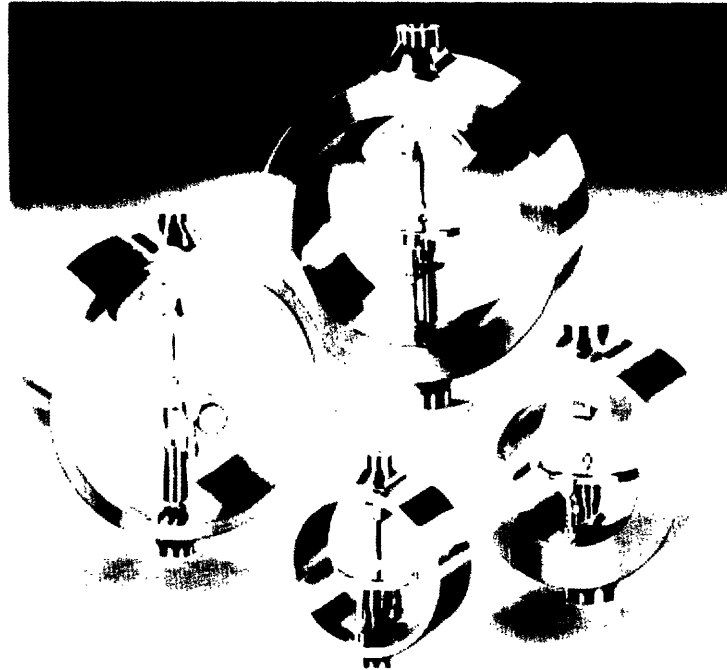


Figure 1: Picture of a classic proving ring force sensor design [1].

A proving ring is a circular hoop of metal intended to measure the force undergone during diametral loading. Diametral loading is defined as the loading that occurs when a hoop, sphere, or cylinder is loaded along the diameter of the object. Figure 2 represents the effect of diametrically loading a proving ring via either compression or tension.

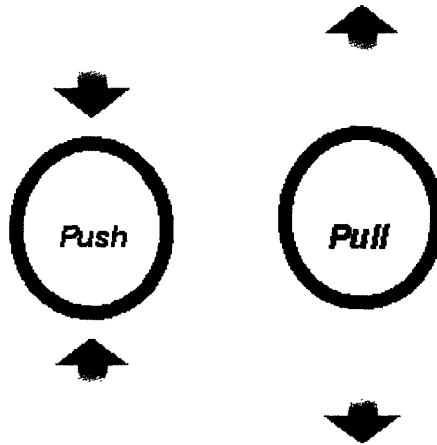


Figure 2: Diagram of the deformation of a diametrically loaded proving ring [1].

Due to the simplicity of the Proving Ring's hoop-like design, if the total deflection of the ring under loading is known, it is possible to numerically solve for the force being applied to the ring. Previous proving ring designs have utilized several different methods of measuring the deflection and include strain gauges, micrometers, and micrometer + vibrating reed combinations.

### 3.2 Prior Art in Proving Ring Force Sensors

The original proving ring was patented in 1929 by S.N Potrenko and H.L. Whittemore [1]. World War I had caused a rapid expansion of industrial processes and it became increasingly important to be able to effectively characterize materials for use in planes, bombs, buildings, and bridges. At the time, there was no way to accurately and repeatedly measure forces. Realizing this incredibly deficiency in the engineering process, S.N. Potrenko proposed that a circular hoop of metal be used such that if one was able to measure its deflection, they would be able to calculate the load being applied to it. Until the advent of digital electronics, the proving ring was one of the most effective methods of measuring forces with high accuracy and high repeatability.

Historically, there have been three ways to measure the deflection of a proving ring:

*Vibrating Reed and Mechanical Micrometer:* The original design of the proving ring consisted of a vibrating reed and a micrometer. The user would first apply the load to the proving ring, then set the vibrating reed in motion with a pencil. The micrometer would then be slowly turned until the tip of the vibrating reed came into contact with the micrometer. At this point, the reed ceased to vibrate and the micrometer was read to determine the deflection of the proving ring.

*Center Mounted Micrometer Proving Ring:* The second generation of proving ring force sensors consisted of a micrometer (first analog, then digital), mounted along the diametrically loaded axis. As the proving ring was loaded, the user merely read the micrometer to determine the deflection of the entire ring.

*Strain Gauge Based Proving Ring:* Another method of measuring the deflection in a proving ring is to mount strain gauges along the non-loaded diametral axis. The output voltages from the strain gauges are then amplified and read using a data acquisition system.

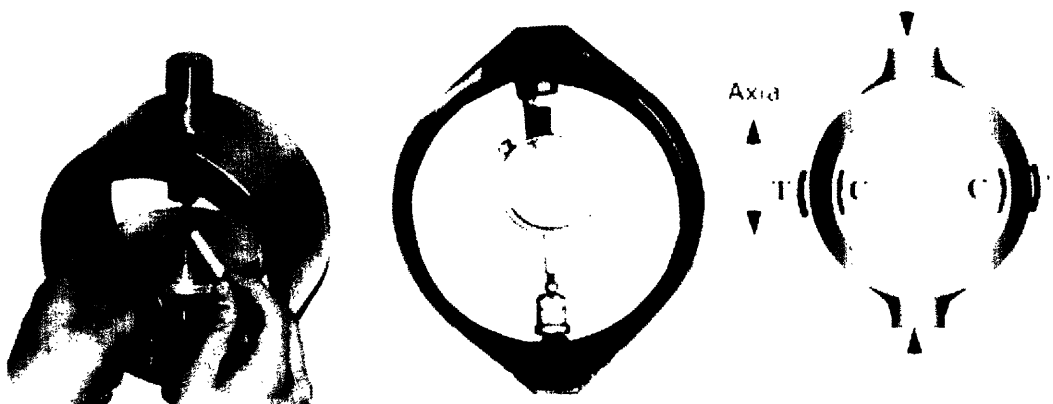
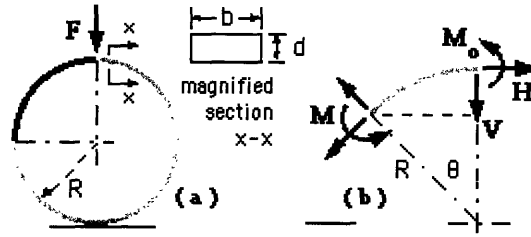


Figure 3: Proving Rings: Reed [1], Micrometer [2], and Strain Gauge [3].



### 3.3 Proving Ring Theory



**Figure 4:** A diagram of the forces experienced by a diametrically loaded proving ring [4].

When analyzing a proving ring under loading, it is easiest to analyze the forces by first analyzing the forces on a thin quarter circle curved beam. Here, the force experienced by the end of the curved beam is  $V$ , which is half of the original force applied to the whole ring, or  $F/2$ . The equation for the moment  $M$  at an arbitrary angle  $\theta$ , is shown by [4],

$$\Sigma M = M + M_o - VR\sin(\theta) - HR(1 - \cos(\theta)) = 0, \quad (1)$$

where  $R$  is the radius of the circle,  $V$  is one half of the total load or  $F/2$ ,  $M_o$  is the moment at the end of the cantilevered beam, and  $H$  is the reaction force at the tip of the beam. Due to the symmetry of a complete proving ring, the net force at the tip of the beam must be zero. Therefore we can state that  $H=0$ . Therefore, solving equation 1 using  $H=0$  we can see that the equation for the moment  $M$  changes to [4],

$$M = VR\sin(\theta) - M_o. \quad (2)$$

Furthermore, taking the partial derivative of  $M$  with respect to  $V$ , and  $H$ , we can see that [4],

$$\partial M / \partial V = R\sin\theta \quad , \quad \partial M / \partial H = R(1 - \cos\theta). \quad (3, 4)$$

We now refer to Castigliano's theorem for an elastic loaded beam. Castigliano's theorem [4] states that,

$$\delta_G = \int_{\text{length}} (M/EI)(\partial M / \partial G) ds, \quad (5)$$

where  $\delta_G$  is the deflection due to an arbitrary load  $G$ ,  $E$  is the Young's Modulus of the material being loaded, and  $I$  is the moment of inertia of the geometry under load. Substituting equations 3 and 4 into Equation 5 (Castigliano's Theorem) we can now solve for the deflection of the system as a function of the loads  $V$  and  $H$ . Thus the deflection equations now become [4],

$$\delta_v = (\pi/4 VR - M_o) (R^2) / EI, \quad (6)$$

and,

$$\delta_h = (VR/2 - (\pi/2 - 1)M_o) (R^2) / EI, \quad (7)$$

where  $\delta_v$  and  $\delta_h$  are the deflections in the V and H directions respectively. However, due to the fact that the proving ring forms a complete circle, the  $M_o$  term must be equal to zero due to the constraints of the system, and V is actually  $V = F/2$  due to the symmetry of the system. Finally, we can rewrite equations 6 and 7 as [4],

$$2 \delta_v = (\pi/4 - 2/\pi) F(R^3)/EI, \tag{8}$$

and,

$$2 \delta_h = (2/\pi - 1/2) F(R^3)/EI. \tag{9}$$

For a proving ring with a hoop thickness of D, and a width B, the moment inertia I, can be found using the following equation [5],

$$I = B(D^3)/12. \tag{10}$$

Therefore, we now have a correlation for a proving ring that relates the total deflection of the ring to the geometry, the material of the ring, and the load applied to the ring. Thus, using equations 8 and 9, if one is able to accurately measure the deflection of the proving ring, they will be able to solve for the load applied to the proving ring.

### 3.4 Hall Effect Sensors and Theory

Hall effect sensors are robust, low cost, non-contact sensors that are capable of measuring magnetic fields produced by magnets, electrical currents, or ferromagnetic materials. Due to their high resolution and sensitivity, they are well suited for high accuracy displacement measurements. Furthermore, because hall effects sensors measure only the magnetic field present, they are well suited to harsh or dirty environments where optical sensors wouldn't work. A diagram of the Hall-effect is shown below.

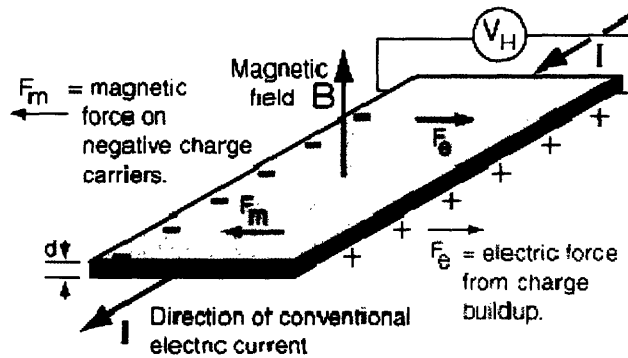


Figure 5: A diagram of the Hall-effect [6].

As Figure 5 demonstrates, hall-effect sensors consist of a thin metal plate through which an input current (I) is applied. When a magnetic field (B) is applied normal to the plane of the metal plate, the electrons passing through the plate are pushed to one side, creating a voltage differential between the two sides of the plate. This voltage ( $V_h$ ) can then be measured and correlated with the applied magnetic field based upon the input current and the dimensions and material of the thin plate. As the size of the plate has no effect of the

accuracy of the hall effect sensor, most hall effects sensors are quite small and are on the order of  $3\text{mm} \times 3\text{mm} \times 2\text{mm}$ . The diagrams in figure 6 show the internal workings of a hall-effect sensor as well as a hall effect sensor in relation to a multi-pole magnet.

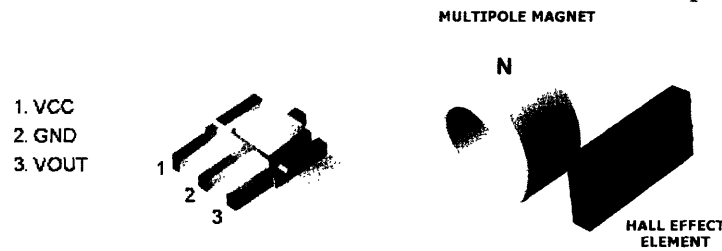


Figure 6: Hall-effect sensors [7].

Specifications: For the purposes of this project, the Honeywell series SS495A Hall-effect sensor was used<sup>1</sup>. When ordered in bulk, a single SS495A costs \$1.69. These sensors also have an incredibly low temperature drift as well as a null output voltage that varies linearly with the input voltage. Furthermore, these sensors have a true DC output voltage that varies linearly with the applied magnetic field. Figure 7 demonstrates these characteristics.

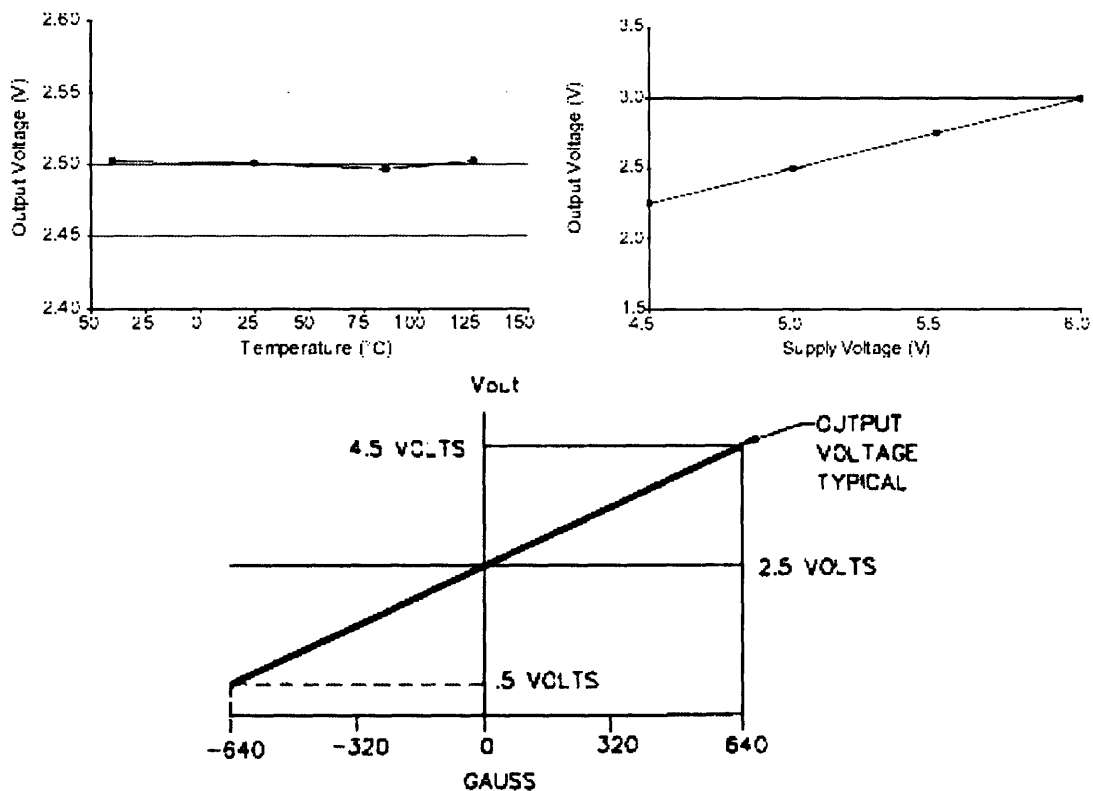


Figure 7: Graph of SS495A Hall-effect sensor characteristics [7].

<sup>1</sup> www.honeywell.com

**SS495 SPECIFICATIONS,  $V_s = 5.0\text{ V}$ ,  $T_A = -40\text{ to }+125^\circ\text{C}$  (unless otherwise noted)**

Catalog Listings		SS495A* Standard	SS495A1* High Accuracy	SS495A2* Basic
Supply Voltage (VDC)		4.5 to 10.5	4.5 to 10.5	4.5 to 10.5
Supply Current @ 25 C (mA)	Typ.	7.0	7.0	7.0
	Max.	8.7	8.7	8.7
Output Type (Sink or Source)		Ratiometric	Ratiometric	Ratiometric
Output Current (mA)				
Typ. Source	$V_s > 4.5\text{V}$	1.5	1.5	1.5
Min. Source	$V_s > 4.5\text{V}$	1.0	1.0	1.0
Min. Sink	$V_s > 4.5\text{V}$	0.6	0.6	0.6
Min. Sink	$V_s > 5.0\text{V}$	1.0	1.0	1.0
Magnetic Range	Typ.	-670 to +670 Gauss (-67 to +67 mT)		
	Min.	-600 to +600 Gauss (-60 to +60 mT)		
Output Voltage Span	Typ.	0.2 to (Vs - 0.2)	0.2 to (Vs - 0.2)	0.2 to (Vs - 0.2)
	Min.	0.4 to (Vs - 0.4)	0.4 to (Vs - 0.4)	0.4 to (Vs - 0.4)
Null (Output @ 0 Gauss, V)		$2.50 \pm 0.075$	$2.50 \pm 0.075$	$2.50 \pm 0.100$
Sensitivity (mV/G)		$3.125 \pm 0.125$	$3.125 \pm 0.094$	$3.125 \pm 0.156$
Linearity, % of Span	Typ.	-1.0%	-1.0%	-1.0%
	Max.	-1.5%	-1.5%	-1.5%
Temperature Error Null Drift (%/C)		$\pm 0.06\%$	$\pm 0.04\%$	$\pm 0.07\%$
Sensitivity Drift (%/C)	$\geq 25\text{ C Max.}$	$-0.01\% + 0.05\%$	$-0.01\% + 0.05\%$	$-0.02\% + 0.06\%$
	$< 25\text{ C Max.}$	$-0.00\% + 0.06\%$	$-0.00\% + 0.06\%$	$-0.01\% + 0.07\%$

Figure 8: Table of SS495A Hall-effect sensor characteristics [7].

## 4.0 Mechanical Design and Finite Element Analysis

The initial analysis of our proposed sensor determined that a proving ring base, combined with hall-effect sensors to measure displacement, could potentially satisfy all of our design criteria outlined in section 3.0. However, the exact design of the proving ring, combined with the accurate placement of the Hall-effect sensors, would inevitably determine the true performance of our manufactured sensor. Realizing that Hall-effect sensors would be used to measure displacement, it was then necessary to determine how many Hall-effect sensors to use, as well as where they should be placed with respect to the proving ring structure.

### 4.1 Dual Differential Design

In our efforts to make as accurate of a sensor as possible, a dual differential measurement system was proposed. According to this proposal, four independent Hall-effect sensors as well as four magnets, would be used to accurately measure the deflection of the proving ring along two independent perpendicular axis. This configuration, shown in Figure 9, would enable force measurements along two axis, as well as temperature compensation and noise reduction due to the differential nature of measuring the displacement along a single axis twice. Mounting four sensors in this configuration creates a very difficult problem as to how to mount the sensors to the proving ring. For all four sensors to independently measure deflection along their respective axis, it is necessary that they all be mounted in such a way that they remain at the relative center of the proving ring, no matter how the proving ring is deformed.

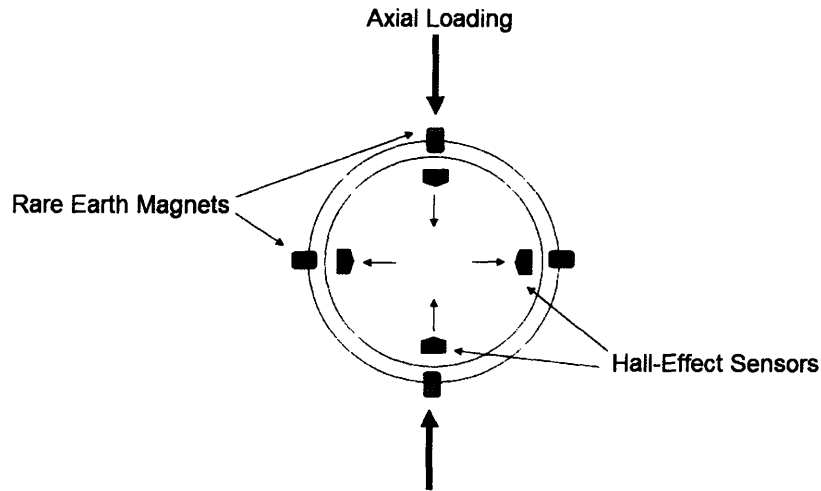


Figure 9: Dual differential Hall-effect proving ring design.

#### 4.2 Novel Nested Proving Ring Design

After dozens of iterations and finite element analysis (FEA), a flexure design was finally developed that fulfilled the design requirement of maintaining all of the Hall-effect sensors at the relative center of the proving ring. This design consists of an outer proving ring with tabs such that the magnets can be mounted directly to the proving ring. The novel flexure design on the inside however is what differentiates our design from that of a standard proving ring. While the outside of the ring represents a standard proving ring design, on the inside there are four smaller proving rings, two for each major axis to be loaded. This nested proving ring design, as shown in Figure 10, enables exact center of the proving ring to remain stable as the proving ring deflects around it.

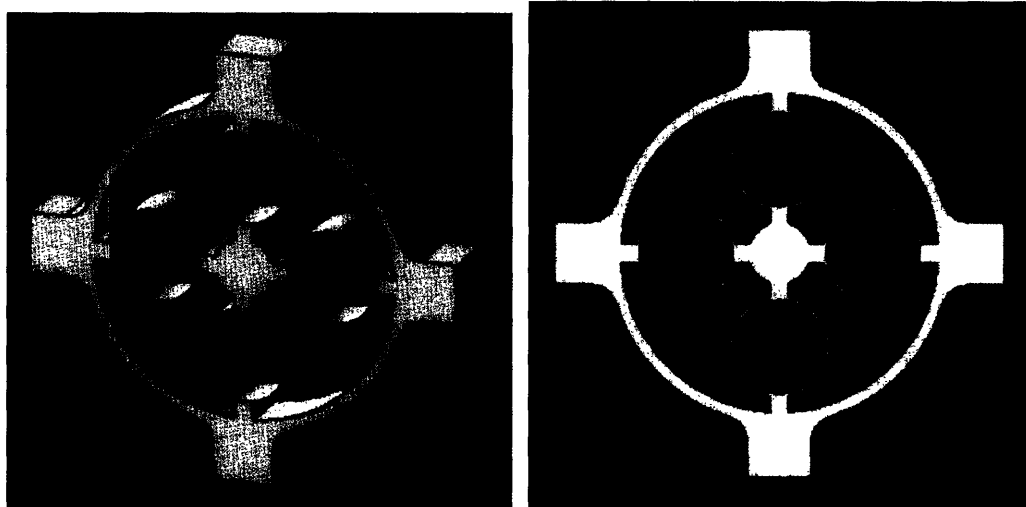


Figure 10: Novel nested proving ring design

The center post, shown in Figure 10, is where the circuit board is to be mounted. The tabs on the outside are where the magnets are to be mounted.

In order to demonstrate the efficacy of the proposed mechanical design, several FEA tests were performed utilizing various loading conditions. These tests, shown in figure 11, demonstrate the deflection characteristics of the proposed nested proving ring flexure. The FEA tests also provide a numerical method of measuring the deflection of the nested geometry under a particular load. As demonstrated above however, the deflection under load of a proving ring is easily characterized and can be solved analytically. For the analysis in this report, the SolidWorks Cosmos<sup>2</sup> finite element package was used. Figure 11 below demonstrates some results of the FEA analysis of the nested proving ring. The FEA analysis proved that the nested proving ring design was in fact capable of maintaining the center of the device stable while the outer proving ring deformed around it. As is shown below in Figure 11, the center of the device remains in the geometric center of the device no matter how the outer proving ring deflects around it.

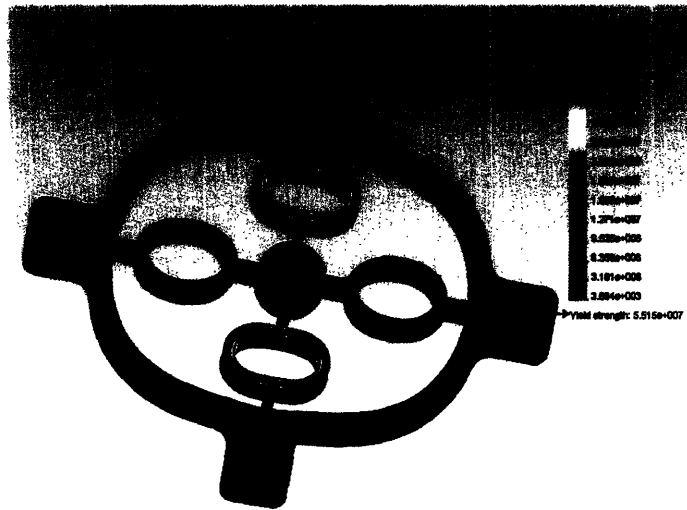


Figure 11: FEA analysis of nested proving ring design.

## 5.0 Device Manufacture, Testing, and Data

Having analyzed the proposed mechanical design and verified its ability to fulfill the required design specifications, I then began prototyping several generations of the sensor. Four different generations of the sensor were completed until the final iteration performed according to the design specifications. The four generations of the sensor were manufactured using three different techniques, laser cutting, 3-D printing, and wire EDM manufacturing.

### 5.1 Hall-Effect Sensor Characterization

Before using the Honeywell SS495A sensors in a prototype, it was necessary to characterize their performance with respect to the particular magnets used for this project. For this project, axially magnetized Neodymium (NdFeB) magnets were purchased from [kjmagnetics.com](http://kjmagnetics.com) at a price of \$0.14 per magnet. The particular magnets used in this

---

<sup>2</sup> [www.solidworks.com](http://www.solidworks.com)

project were of a cylindrical shape  $1/8^{\text{th}}$  inch in diameter and  $1/8^{\text{th}}$  inch long. Figure 12 shows the D22 NdFeB magnet next to a penny.



**Figure 12:** The D22  $1/8^{\text{th}}$  Inch Rare Earth (NdFeB) Magnet [8].

The D22 magnet shown above has a mass of 0.189 g, a pull force of 4 N, and a surface flux of 0.354 T.

In order to test the hall-effect sensors, a single D22 magnet was mounted to a micrometer and placed in close proximity to a single SS495A hall-effect sensor. The hall-effect sensor was supplied with 6.0V DC from an Agilent E3630A power supply. The voltage output from the hall-effect sensor was recorded with an Agilent 34970A<sup>3</sup> data acquisition unit set to 6.5 digits of precision. A diagram of the hall-effect sensor characterization setup is shown below.

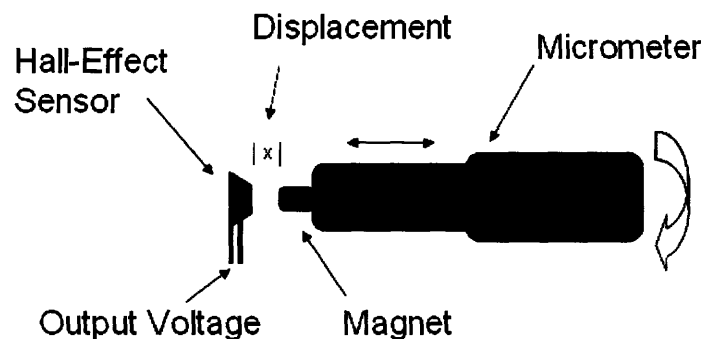


**Figure 13:** Hall-effect sensor characterization setup.

At the onset of the experiment, the hall-effect sensor was placed directly in contact with the magnet. However, the SS495A hall-effect sensors have a maximum magnetic flux rating of 0.064 T. Accordingly, the micrometer was turned to move the hall-effect sensor away from the magnet until non-zero output voltage was recorded coming out of the sensor. The experiment indicated that the magnetic field had fallen off to 640 Gauss after 1.75mm. The hall-effect sensor was then slowly moved away from the magnet at discrete increments of .25mm and the voltage output of the sensor was recorded. Figure 14 shows the output voltage of the SS495A hall effect sensor as a function of its distance from a single D22 NdFeB  $1/8^{\text{th}}$  inch magnet.

<sup>3</sup> [www.agilent.com](http://www.agilent.com)

## Vout (V) vs. Distance (mm)

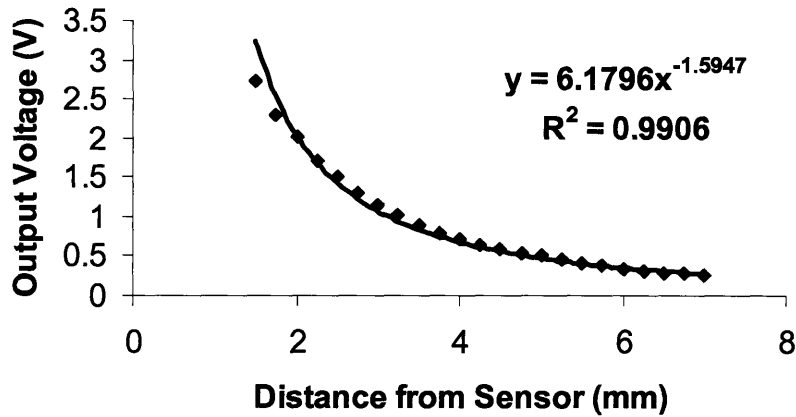


Figure 14: Characterization of the SS495A Hall-effect sensor.

The data was fitted with a power trend-line and the resulting fit is shown in figure 14. Due to the fact that the SS495A hall-effect sensors voltage output is linear with respect to the magnetic field, graph 14 in reality demonstrates the manner in which any magnetic field falls off as a function of the radius from the source. As can be seen in figure 14, the magnetic field falls off as a function of  $\sim R^{1.5}$ . The graph also demonstrates the point at which the magnetic field is too strong for the SS495A sensor and accordingly no data points are recorded in the 0-1.75mm range.

As the graph in Figure 7 demonstrates, if the SS495A sensor is powered with a 6 V input, its null output, the output in the absence of a magnetic field, will be 3 V. This is why the output voltage in Figure 14 drops from 3 V to nearly 0 V. However, Hall-Effect sensors are capable of sensing both positive and negative magnetic fluxes (north and south poles), and accordingly the output voltage of the sensor varies with the pole of the magnet that it is being exposed to. Figure 14 demonstrates the sensor's response to the north pole of a D22 magnet while Figure 15 below demonstrates the response of a SS495A sensor to both the north and south pole of a D22 magnet. Notice the symmetry about the null output voltage, 3 V.



### SS495A Response Characteristics

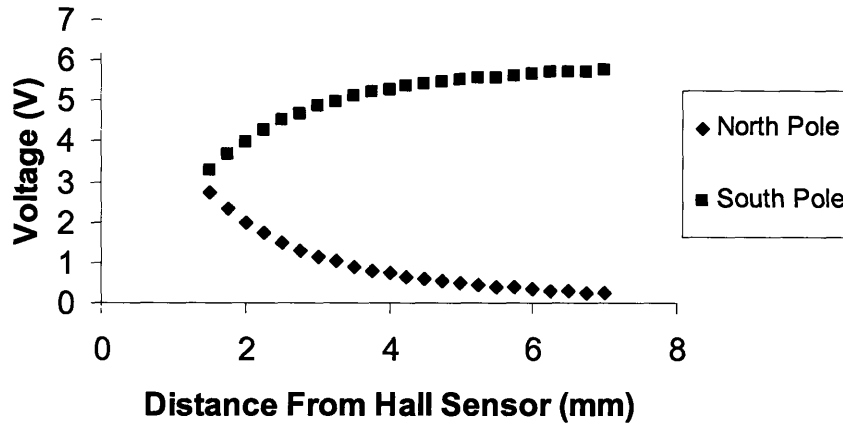


Figure 15: SS495A Hall-effect sensor's response to North and South poles.

Proper characterization of the performance of the Hall-effect sensors will be critical to effectively evaluating the performance of the completed proving ring sensor. Having determined the output voltage of the SS495A sensor as a function of distance from a D22 magnet, it is then possible measure the deflection of the nested proving ring apparatus merely by measuring the output voltage of the SS495A sensor. However, it is first necessary to effectively mount both the Hall-effect sensors, as well as the magnets, onto the nested proving ring base.

### 5.2 Circuit Board Design

In order to mount the Hall-Effect sensors to the mechanical design proposed in Figure 10, it was first necessary to design a circuit board onto which the hall-effect sensors would be mounted. The circuit board would then be mounted to the center post of the nested design such that the entire circuit board, Hall-Effect sensors include, would remain centered relative to the deflection of the proving ring around it. The program ExpressPCB was used to design the circuit board and the circuit boards were purchased through ExpressPCB's online ordering system<sup>4</sup>. Figure 16 shows the ExpressPCB drawing of the circuit board as well as a solid model of what the circuit board will look like when attached to the nested proving ring base. The circuit board is to be mounted to the proving ring by being glued to the center post of the nested proving ring design. This ensures that the entire circuit board will remain centered as the proving ring deflects around it.

<sup>4</sup> [www.expresspcb.com](http://www.expresspcb.com)



**Figure 16:** Circuit board design and implementation.

As shown in Figure 16, the circuit board has two mounting positions for each Hall-effect sensor such that their distance relative to the magnets can be changed if needed. Furthermore, each sensor is connected to a common voltage and a common ground, yet each sensor has its own  $V_{out}$  take-off point. The right side of Figure 16 demonstrates what the completed sensor might look like when combined with an onboard processor.

### **5.3 Generation 1: Laser Cut 10mm Acrylic**

Having performed the relevant FEA analysis, it was time to build a physical mock-up prototype to demonstrate the physical characteristics of the device. A solid model similar to those shown in figures 10 and 16 was developed from which a 2 dimensional drawing was created. This drawing was then imported into Corel Draw on the Trotec Laser Ingraver<sup>5</sup>. Cutting out the geometry from a 10mm thick clear acrylic sheet, the laser engraver was used to create a scale model of the nested proving ring design. This initial physical prototype is shown below in Figure 17. This first generation was never intended to be a functional device but instead was meant to serve as a visual and tactile aid. However, this first generation cut out of acrylic was effective in demonstrating the size, shape, and feel of the nested proving ring design. Furthermore, this first generation, while never rigorously tested, did demonstrate the desired flexural characteristics stated in the original design.

---

<sup>5</sup> [www.trotec.net](http://www.trotec.net)

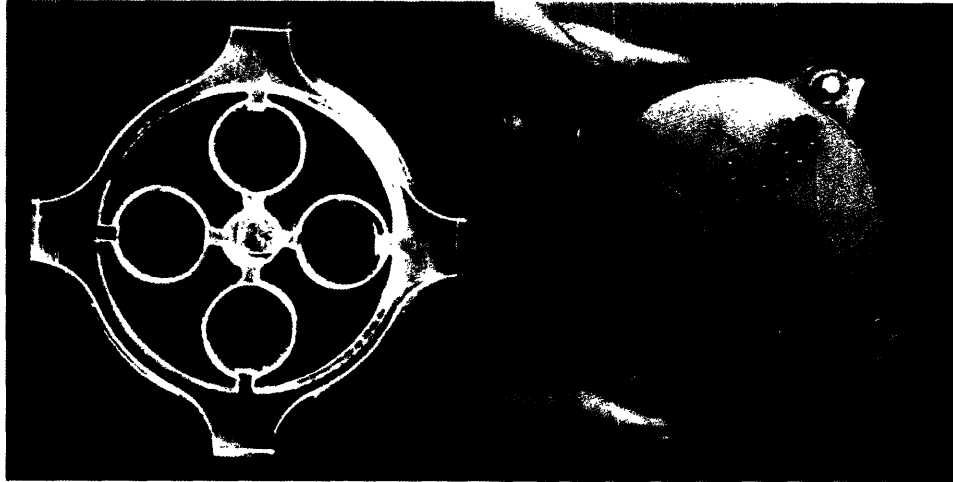


Figure 17: First generation laser cut acrylic nested proving ring.

As can be seen in Figure 17, the center post is slightly elevated such that the circuit board can be glued and not interfere with the deflection of the proving ring.

#### **5.4 Generation 2: 3D Printed Viper Resin**

The second generation of the device was fabricated using the Viper Resin 3D printer. SolidEdge was used to develop a solid model which was then imported into Lightyear 1.4. The Lightyear .bff file was then loaded onto the 3D printer and two copies of the device were printed, cleaned, and UV hardened. Figure 18 below shows the result of the 3D printing on the left and the same device after the circuit board has been attached and wired on the right. Note that due to the ease of creating complex geometries with the 3D printer, vertically oriented magnet holders were integrated into the body of the nested proving ring. The result is shown below.

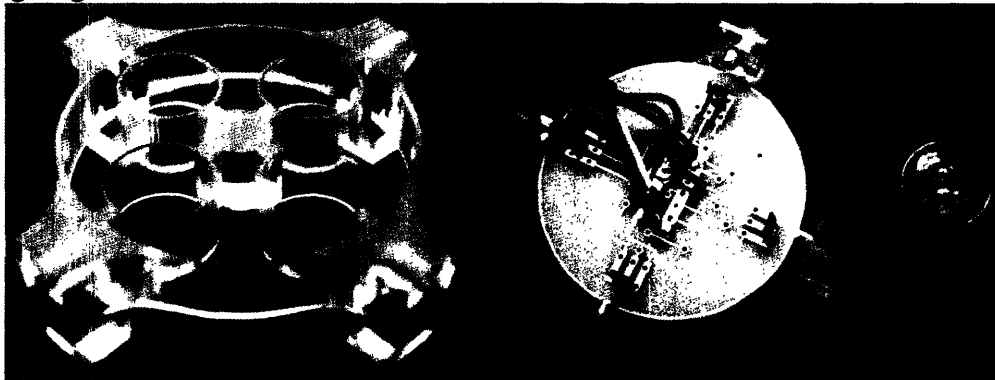
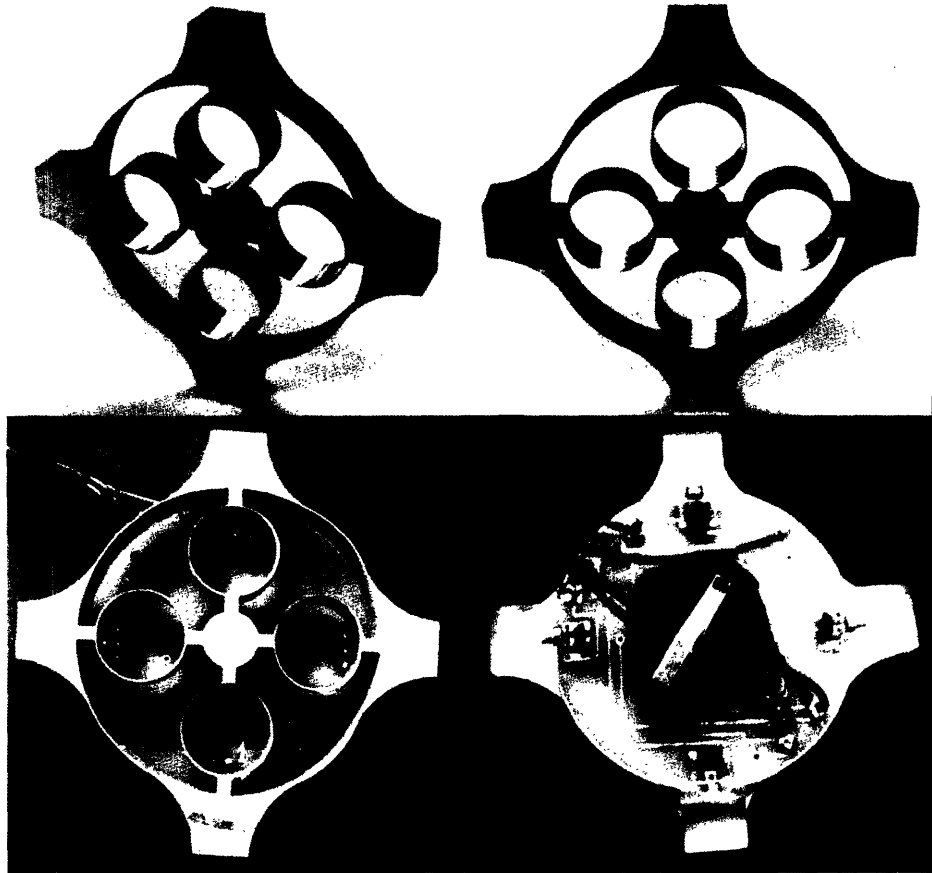


Figure 18: Second generation 3D printed nested proving ring.

### **5.5 Generation 3: Wire EDM, Low Force Aluminum Proving Ring**



**Figure 19: Third generation wire EDM manufactured proving ring**

The next generation of proving ring manufactured was a thin-walled low force proving ring made out of 6060 grade aluminum. Unlike the previous two generations, the manufacture of this first generation of aluminum proving ring was a much more involved process requiring high precision machining as well as the utilization of a wire EDM. A 3-axis CNC Hass machining center was used to mill eight holes, four in the center of the smaller, nested proving rings, and four smaller holes in the negative space of the interior of the larger proving ring. The wire of the wire EDM was then fed through these smaller holes and utilized to cut out the rest of the internal geometry of the proving ring. The wire EDM was then used to cut the external geometry around the proving ring thus freeing the proving ring from its aluminum stock. As can be seen in Figure 19, the walls of this iteration of the proving ring are very thin - only 300 micrometers. Unlike the 3D printing process, when manufacturing the aluminum proving ring it was not possible to incorporate the vertical magnet holders into the manufacturing process of the aluminum. Accordingly, as can be seen in Figure 19, a 3D printer was used to manufacture the vertical magnet holders, which were then glued onto the aluminum base.

### **5.6 Generation 4: Wire EDM, High Force Aluminum Proving Ring**

The fourth generation of the proving ring was manufactured in exactly the same manner as generation 3. However, in this iteration, the walls of the proving ring were designed to

be much thicker enabling a much higher force proving ring. The walls thickness of this generation was 1.5mm for the larger outside proving ring and .4mm for the smaller, nested proving rings. As with all of the other generations as well, the inner diameter of the larger proving ring was 25mm while the inner diameter of the nested proving rings was 10mm.

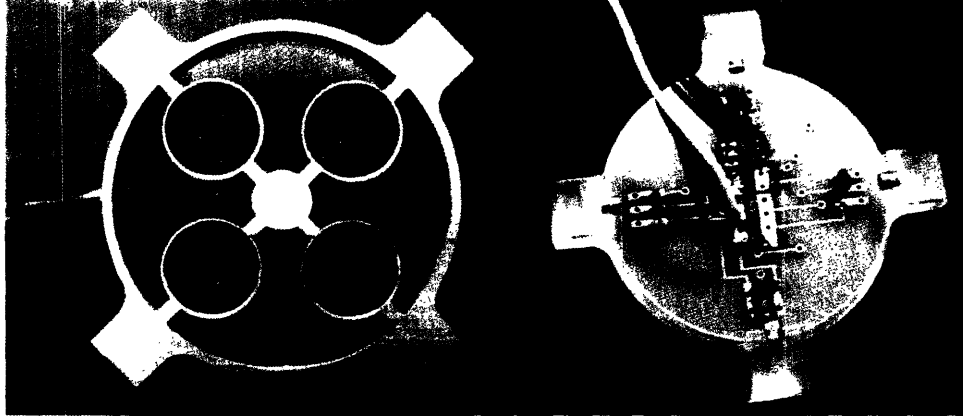


Figure 20: Fourth generation wire EDM manufactured proving ring.

## 6.0 Experimental Setup

Having manufactured 4 generations of nested proving ring force sensors, it was then necessary to test them and to characterize their performance. In order to test the sensors, an experiment was set up in which accurate brass masses were attached to the sensor and the sensor was then hung on a hook attached to a horizontal pole. By varying the number of masses attached to the proving ring, it was possible to quickly and easily apply a know load in a tensile manner to the proving ring. During this process, all of the hall-effects sensors were supplied with a 6 volt input signal supplied by an Agilent E3630A Power Supply. The output voltage of each sensor was then read using an Agilent 34970A Data Acquisition System set to six and a half digits of precision. As the load on the proving ring was increased by adding masses in increments of 0.2kg, the output voltage was measured and tabularized in Microsoft Excel. The output voltage was then converted into a displacement using the equation shown in Figure 14. A photograph of the experimental setup is shown in Figures 21 and 22.

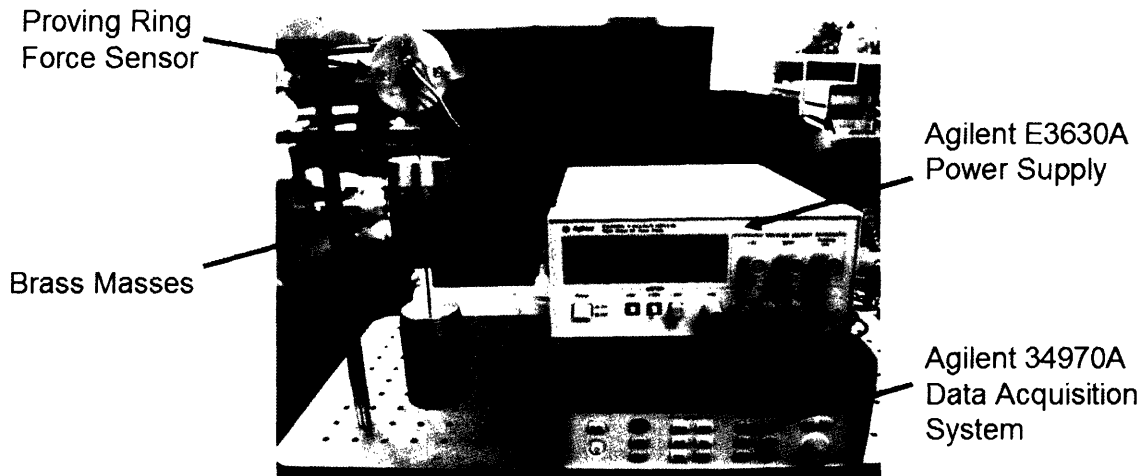


Figure 21: Experimental setup.

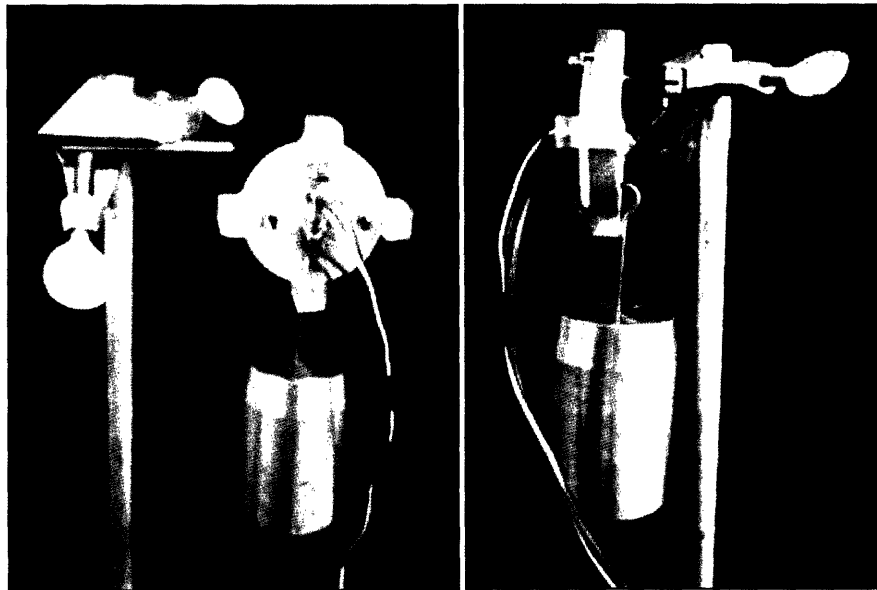


Figure 22: Close up of experimental setup.

## 7.0 Testing, Data, and Analysis

The purpose of testing these devices is to assess how accurately they measure the load applied to them. As force sensors, it is critical that they are able to measure forces accurately and repeatedly. However, it is first necessary to create a benchmark against which the test results of each sensor can be compared. Accordingly it was necessary to develop a predictive model for the nested proving ring design. Based on our knowledge of how the hall-effects sensors respond to the D22 magnets, and based on our knowledge of how a theoretical proving ring deflects under load, it is then possible to develop a theoretical model for the nested proving ring design against which our test results can be compared.

In section 3.2 an analysis was performed for the manner in which a single proving ring should deflect under a given load. In order to develop an accurate model, it is necessary to perform a similar analysis on the entire nested proving ring design. We must

determine how the addition of nested proving rings affects our load equations, Equations 8 and 9. To do so, we can model the nested proving ring design as a single larger proving ring containing four springs in its interior. The spring constant of each of these “springs” or nested proving rings, can be determined using the deflection equations 8 and 9. A model of the nested design is shown below.

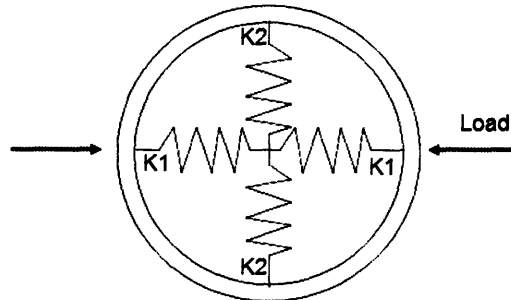


Figure 23: Spring model of nested proving ring design.

As can be seen in Figure 23, each nested proving ring along a similar axis can be assumed to have the same spring constant as the other nested proving ring on the same axis. As with all springs in series, the total spring constant in each axis can therefore be assumed to be half that of a single nested proving ring. Utilizing Equations 8 and 9, we can create graph of the load versus the displacement for the larger outer proving ring as well as the smaller nested proving rings. For the purposes of this model, the diameter of the large proving ring was set at 52 mm with a wall thickness of 1.5 mm and a depth of 10 mm. The small nested rings were assumed to have a diameter of 10mm and a wall thickness of 0.4mm. The slope of the lines in this graph will represent the effective inverse spring constant, in units mm/N, of the various sized proving rings. Figure 24 shows a graph of the inverse spring constant (mm/N) for both the larger outer proving ring as well as the smaller inner proving ring.

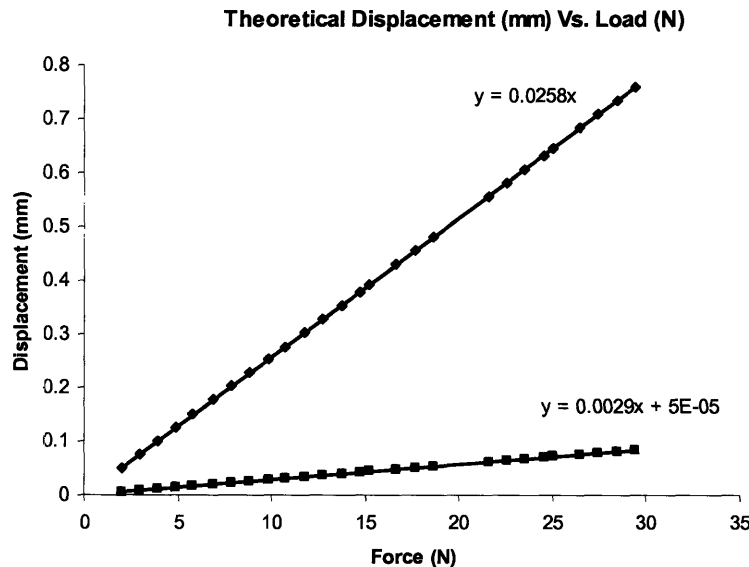


Figure 24: Inverse spring constants for outer and inner rings.

By taking the inverse of the slopes in this graph we can therefore calculate the effective spring constant of the large and small rings. The large ring was determined to have a spring constant of 344.82 N/mm while the small ring was determined to have a spring constant of 38.75 N/mm. However, because the two small rings are in series, the sum of the spring constants along a single axis is actually half of that for a single ring, or 19.37 N/mm. Therefore, because the wall thickness of the inner rings is small in comparison with the larger ring, the total spring constant of these inner rings is less than 5% of that of the larger ring. Accordingly, in making our model it is safe to assume that the effect of the nested proving rings on the load versus displacement characteristics of the device can effectively be ignored. As one further increases the thickness of the outer ring with respect to the inner rings, the effect of the smaller rings will effectively become negligible. Thus in order to optimize future designs, the outer ring should be significantly thicker than the inner, nested rings.

As shown in Figure 24, we expect that the displacement of the proving ring sensors should vary linearly with the load applied. Having predicted the theoretical performance of the nested proving ring sensors, it was then necessary to test their performance. The devices were tested in the order they were manufactured starting with the 3D printed device.

### 7.1 Generation 2 Testing (3D Printed Sensor)

The 3D printed force sensor was tested using masses of 0.1 to 0.6kg in increments of .05kg. The displacement of each magnet relative to the hall-effect sensor nearest to it was then plotted and can be seen in Figure 25. Notice that the two lines with a positive slope represent the two hall-effect sensors along the loaded axis, while the two negatively sloped lines represent the two hall-effects sensors along the non-loaded axis.

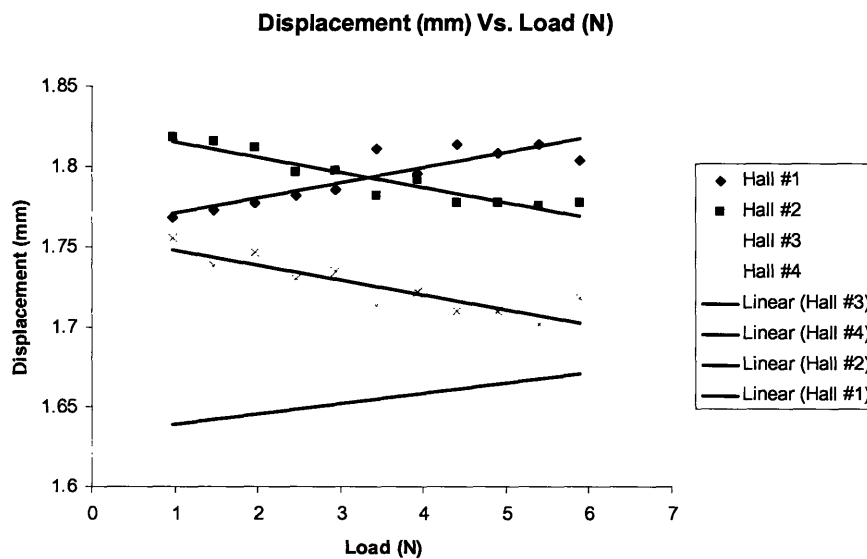
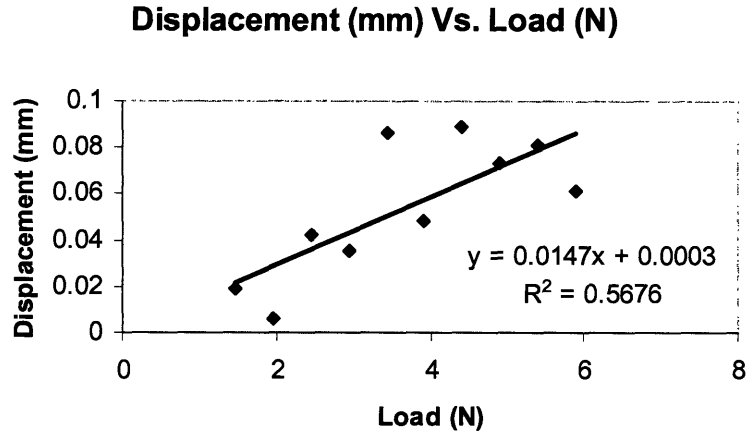


Figure 25: Displacement versus load for 3D printed proving ring.



The data from Figure 25, hall sensors #1 and #3, was then combined and the total displacement along the loaded axis was plotted as a function of the load applied. A graph of this displacement can be seen in Figure 26.



**Figure 26:** Loaded axis displacement versus load, 3D printed sensor.

As shown in Figure 24, we would expect the displacement vs. load graph to be a perfectly linear line, which Figure 26 clearly is not. What this means is that the 3D printed hall-effect force sensor is unacceptably inaccurate. There are several reasons why the 3D printed sensor is inaccurate. First of all, by the nature of the 3D printing process, the material composition of the device is non-uniform, thus leading to a non-linear displacement profile. Second, the Young's modulus of hardened U.V. resin is on the order of 2MPa, making it a very flexible material. By the nature of the loading process, some of the loading may have occurred slightly off-axis. Due to the soft nature of the U.V. resin, this could have caused the sensor to bend in the plane of the device. As we probably could have guessed, the 3D printed force sensor was not effective as an accurate force sensor, accordingly it was necessary to test the aluminum sensors.

### **7.2 Generation 3 Testing (Low Force Aluminum Sensor)**

The low force aluminum proving ring force sensor was loaded in the exact same manner as the 3D printed version. Again, the displacement along the loaded axis was plotted as a function of the load applied and can be seen below in figure 27. As figure 27 demonstrates, the low force aluminum sensor does not respond as we would expect.

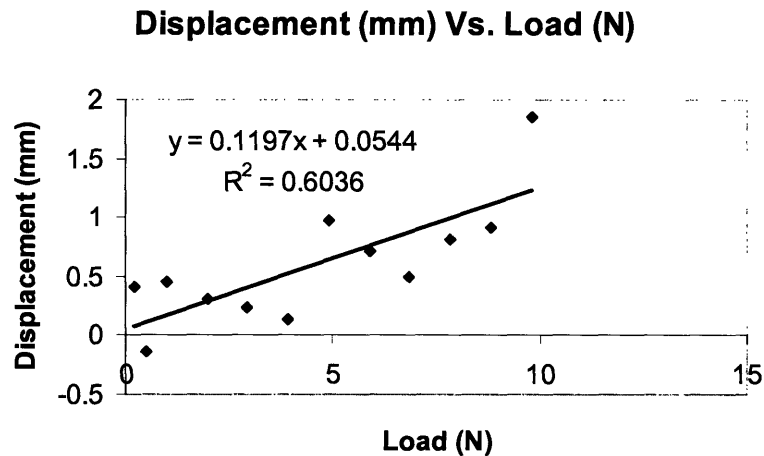


**Figure 27:** Loaded axis displacement versus load, low force aluminum sensor.

After the experiment was completed, the reason for the inaccuracy of this sensor was discovered. Because the wall of this sensor had been manufactured to be only 300 micrometers thick, it was noticed in loading the device the maximum strain limit had been exceeded and part of the exterior proving ring had plastically deformed. Figure 27 below is a photograph of the plastic deformation of the low force proving ring.

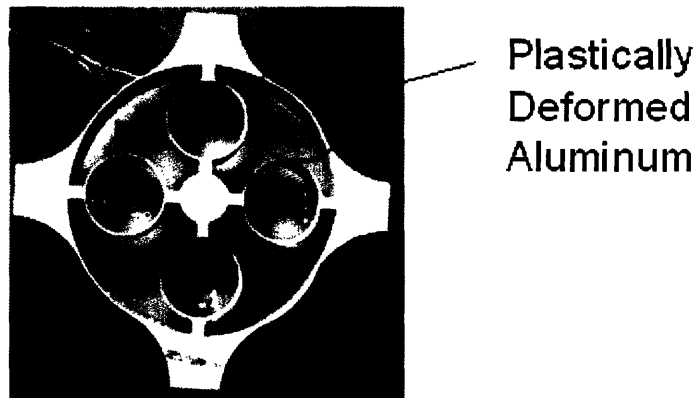


**Figure 28:** Plastically deformed low force proving ring.

#### **6.4 Generation 4 Testing (High Force Aluminum Sensor)**

The fourth generation of the device proved significantly more accurate than the previous generations. Because this sensor was designed to measure higher forces, it was tested with masses from 0.2 kg to 3 kg in increments of 0.1kg. Accordingly to load experienced by the sensor was varied from 1.94 N to 30 N. The position of each Hall-effect sensor was recorded as a function of the load applied and can be seen in Figure 28.

### Displacement (mm) Vs. Load (N)

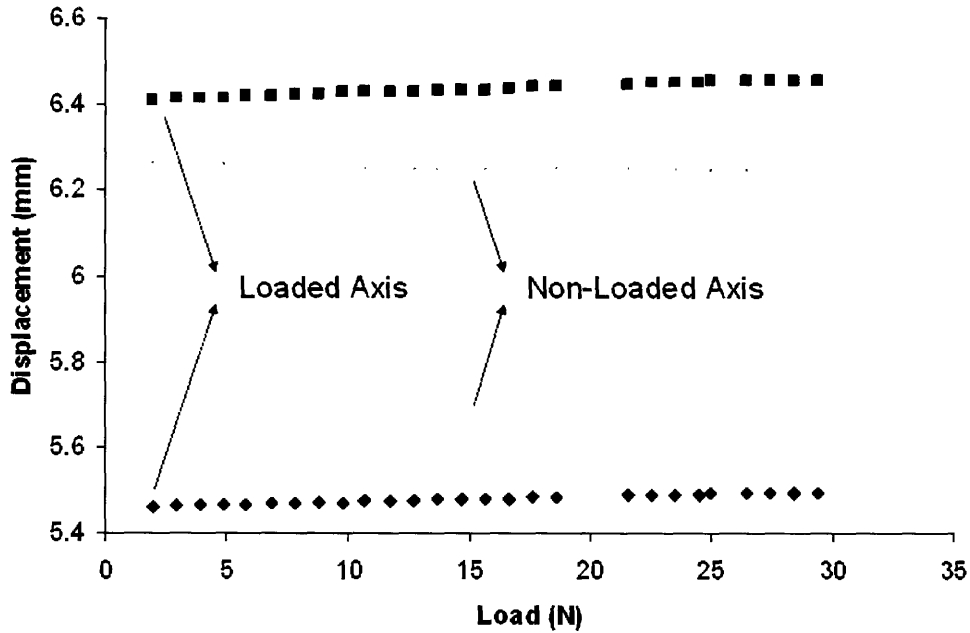


Figure 29: High force Hall-sensor readings.

The data from both hall-effect sensors along the loaded and unloaded axes was then compiled to determine the net deflection of the device along both axes. A graph of the deflection versus the load of each axis was then plotted and each data set was fit with a linear trend-line. This is represented in Figure 29 below.

### Deflection (mm) Vs. Load for both Axes

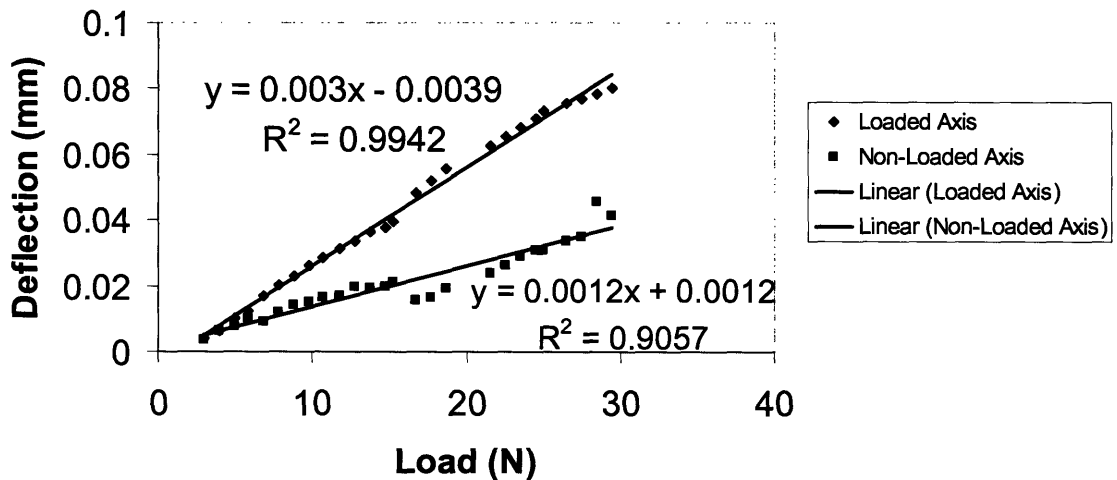
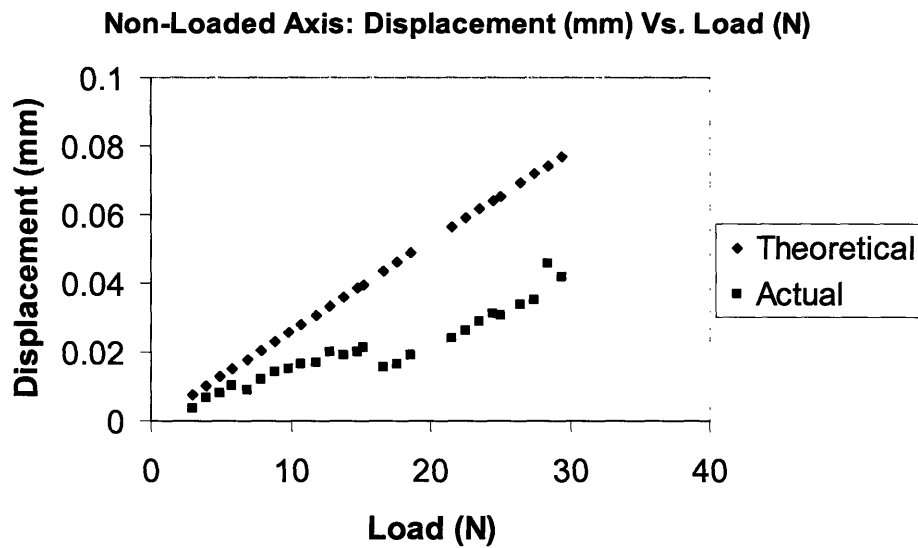


Figure 30: Bi-axial deflection versus load, high force sensor.

As can be seen in figure 29, the loaded axis can be closely approximated as linear as the  $R^2$  value of the fit is 0.9942. The unloaded axis however, is much more irregular and is not well approximated with a linear trend-line as its  $R^2$  value is only 0.9057. This would imply that our recorded data along the loaded axis was highly accurate while the data along the unloaded axis was quite inaccurate. However, it was still necessary to compare the acquired data with a theoretical model. As Equations 8 and 9 demonstrate, it is possible to plot the displacement of a proving ring as a function of the load applied assuming that the geometry and material are known. Accordingly, the data for the deflection along each axis was then compared to what the deflection should have theoretically been, given the high force sensor's dimensions and material composition.



**Figure 31:** Non-loaded axis, theoretical versus actual deflection.

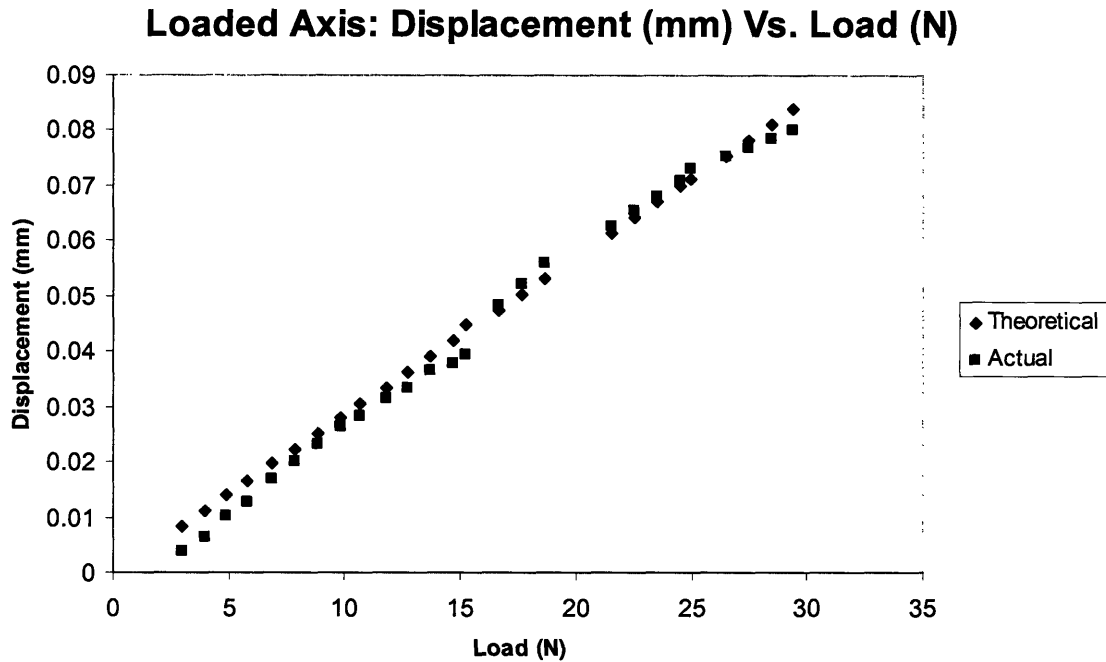


Figure 32: Loaded axis, theoretical versus actual deflection.

As Figures 30 and 31 demonstrate, the high force nested proving ring is highly accurate along the axis under load but produces inaccurate results along the non-loaded axis. The inaccuracy of the data from the non-loaded axis is most likely due to the nested proving ring design: a problem that could potentially be resolved by increasing the ratio of wall thickness of the outer proving ring to that of the inner proving rings.

Statistical analysis was performed on the data set generated by the loaded axis hall-effect sensors and the accuracy of the force sensor along the loaded axis was determined. The deflection results along this axis differed from the theoretical model with a standard deviation of 0.002356 mm. Translating this deflection measurement error into a load measurement error, it was therefore determined that the average recorded load along the loaded axis was off by an average of 3.5%. In other words, the high force sensor had a force resolution of plus or minus 0.235 N, or approximately 23.9 grams, within a tested range of 0 to 30 N.

## 8.0 Conclusions and Further Work

The stated design goal was to build a low cost, accurate, and robust force sensor for use in educational and commercial settings. This was achieved, as outlined in this report, through the unique combination of Hall-effect sensors attached to a nested proving ring base. Having manufactured and characterized several generations of these nested proving ring force sensors, it is clear that this design offers a cheap and simple way to manufacture an accurate force sensor.

Future work should be focused on improving the accuracy of the sensor. This can most likely be achieved in two ways: increasing the wall thickness of the outer proving ring, and increasing the ratio of thicknesses between the inner nested rings and the outer ring. While the high force sensor tested in this report was had an average accuracy of 3.5%, or 0.235 Newtons, it is clear that some slight modifications to the sensor's geometry could significantly increase the sensor's performance. Furthermore, the high force sensor was only tested to a load of 30N but it's strain limit is much higher. Further testing should test the accuracy of the sensor at higher loads as the error percentage is likely to decrease as the load increases.

When mass-manufactured, it is likely that the nested proving ring flexure can be made out of extruded aluminum and cut to the proper thickness. As Hall-effect sensors and magnets are very inexpensive, this would enable the entire device to be manufactured for considerably less than \$10.00 per unit.

Future iterations of the device could potentially be battery powered utilizing on board processors to determine the load applied. Integration of these components onto the circuit board would provide for a highly accurate, low cost wireless force sensor.

A patent disclosure has been filed for the design described in this report.

## References

- [1] National Institute of Standards and Technology Website (NIST):  
[http://www.mel.nist.gov/div822/proving\\_ring.htm](http://www.mel.nist.gov/div822/proving_ring.htm)
- [2] [www.sensorland.com](http://www.sensorland.com)
- [3] <http://www.shambhaviimpex.com>
- [4] <http://www.mech.uwa.edu.au/DANotes/MST/thin/thin.html>
- [5] EfunDa, Engineering Fundamentals: [www.efunda.com](http://www.efunda.com)
- [6] <http://hyperphysics.phy-astr.gsu.edu/hbase/magnetic/hall.html>
- [7] Allegro MicroSystems Inc.: [www.allegromicro.com](http://www.allegromicro.com)
- [8] K and J Magnetics Inc.: [kjmagnetics.com](http://kjmagnetics.com)
- [9] MIT's iCampus Initiative: <http://icampus.mit.edu/>
- [10] BioInstrumentation Lab's IDAT Initiative: <http://idat.mit.edu/>
- [11] W.B.Bickford. *Mechanics of Solids*. Richard D.Irwin, Burr Ridge, Illinois, 1993.
- [12] A. H. Slocum. *Precision Machine Design*. Society of Manufacturing Engineers, originally published by Prentice-Hall, Dearborn, Michigan, 1992.
- [13] Young, W. and Budynas, R., *Roark's Formulas for Stress and Strain, 7th ed.* New York: McGraw-Hill, 2002.